J Mater Sci (2011) 46:7713–7724
DOI 10.1007/s10853-011-5751-x

On the intrinsic ductility of electrodeposited nanocrystalline metals

**I. Brooks · G. Palumbo · G. D. Hibbard ·
Zhirui Wang · U. Erb**

Received: 12 March 2011 / Accepted: 27 June 2011 / Published online: 8 July 2011

Abstract While nanocrystalline materials hold promise for structural applications in which increased strength is beneficial, their adoption has been hindered by concerns over the achievable ductility, resulting largely from considerable data scatter in the literature. A statistically significant set of 147 electrodeposited nanocrystalline tensile specimens was used to investigate this topic, and it was found that while necking elongation obeys similar processing quality and geometrical dependencies as conventional engineering metals, the intrinsic ductility as measured by uniform plastic strain was unexpectedly independent of microstructure over the grain size range of 10–80 nm. This indicates that the underlying physical processes of grain boundary-mediated damage formation are strain-oriented phenomena that can be defined by a critical plastic strain regardless of the strength of the material as a whole.

Introduction

Grain refinement is a well-known metallurgical strengthening mechanism and is governed by the Hall–Petch relationship:

$$\sigma_{\mathrm{Y}} = \sigma_o + kd^{-\frac{1}{2}} \tag{1}$$

where σ_{Y} is yield strength or flow stress, d is the average grain size, and σ_o and k are material constants [1, 2]. Examination of the Hall–Petch equation reveals that grain refinement into the nanocrystalline regime (average grain size < 100 nm) holds promise as a means to achieve substantially increased flow stress in a polycrystalline solid. Hardness follows a similar trend. This effect is the primary driver behind the substantial body of research and commercialization activity that has been undertaken in the field of nanocrystalline materials over the past 25 years or so, with electrodeposition having recently emerged as a preferred technique for the production of bulk quantities of these materials. While much has been written concerning the relationship between grain size and strength [e.g., 3–5] or hardness [e.g., 6–8], the literature contains a great deal of conflicting data regarding the intrinsic ductility and toughness of nanocrystalline materials [e.g., 9–11]. Achievable ductility is a critical piece of information that must be accounted for not only in material formability considerations and the design of reliable load bearing structures, but also in the broader assessment of material quality and damage tolerance. In order to assess the intrinsic ductility of electrodeposited nanocrystalline metals, a statistically significant set of 147 specimens cut from monolithic nanocrystalline Ni-based electrodeposits were tensile tested and analyzed via fractography and two-parameter Weibull distributional analysis of strain-to-failure data.

Experimental

The creation of nanocrystalline materials by electrodeposition is well-established and the most commonly used base metals are Ni, Cu, Co, Fe, and Au [12, 13]. For this

---

I. Brooks (✉) · G. D. Hibbard · Z. Wang · U. Erb
Department of Materials Science and Engineering,
University of Toronto, Toronto, ON M5S 3E4, Canada
e-mail: brooks@integran.com

I. Brooks · G. Palumbo
Integran Technologies Inc., 5300 Northam Drive,
Mississauga, ON L4V 1H7, Canada

Table 1 Composition of Watts-type electrodeposition bath used in this study

Constituent	Concentration (g/L)
$NiSO_4 \cdot 6H_2O$	260–300
$NiCl_2 \cdot 6H_2O$	45
H_3BO_3	45
$FeCl_2 \cdot 4H_2O$	0–35
$Na_3C_6H_5O_7 \cdot 2H_2O$	0–30
Proprietary grain refiner	0.1–10
Proprietary wetting agent	0–15 mL/L

particular study, only Ni-based metals and alloys were scrutinized. The aqueous Watts-type Ni electroplating solution used as the base formulation for this study is included in Table 1. To prepare the 40L electrolyte, standard analytical grade chemicals from Alfa Aesar and Fisher Scientific along with an Atotech proprietary wetting agent and an Integran proprietary grain refining bath additive were added to heated distilled water. The electrolyte temperature was maintained between 60 and 65 °C while the pH was 1.5–2.5. INCO R-rounds were employed as the consumable Ni anode, and this anode material was contained within a bagged Ti basket, as is standard electroplating practice. Pulsed electrodeposition was carried out galvanostatically using cathodic square wave pulses with complete current cut-off during the intervals between the pulses. Cathodic current on-time values ranged from 1 to 20 ms, off-time values ranged from 0 to 100 ms, and peak current density values ranged from 0.2 to 1 A/cm^2 as described in more detail in the work of El-Sherik et al. [e.g., 12–14].

Figure 1 contains TEM characterization data for a typical nanocrystalline Ni electrodeposit of 31 nm average grain size. As discussed elsewhere [14, 15], the microstructure of nanocrystalline electrodeposits typically exhibits a log-normal grain size distribution. The crystal structure, preferred crystallographic orientation, and grain size of electrodeposited nanomaterials is dependent upon the chemical composition and plating parameters of the

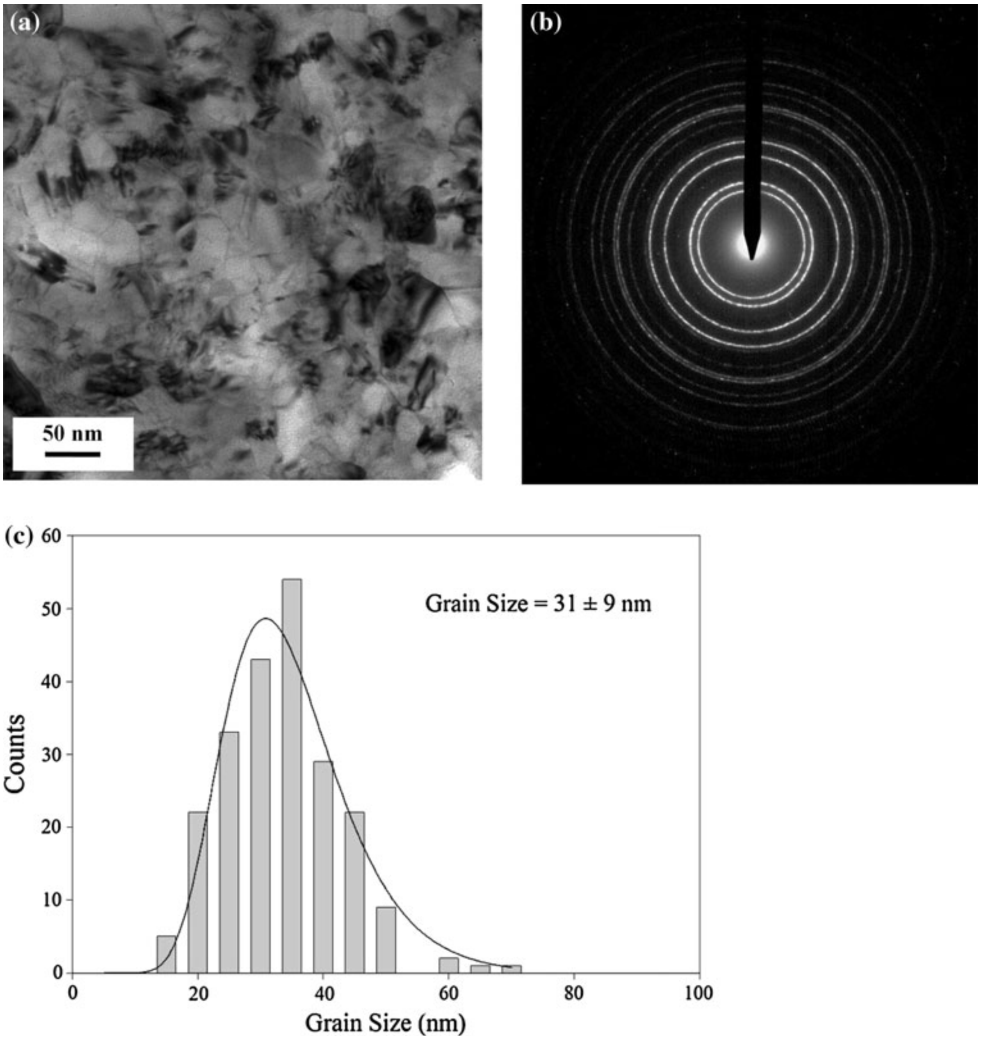

Fig. 1 TEM characterization data of a nanocrystalline Ni (31 ± 9 nm average grain size) sample showing **a** bright field image, **b** selected area diffraction pattern, and **c** grain size distribution

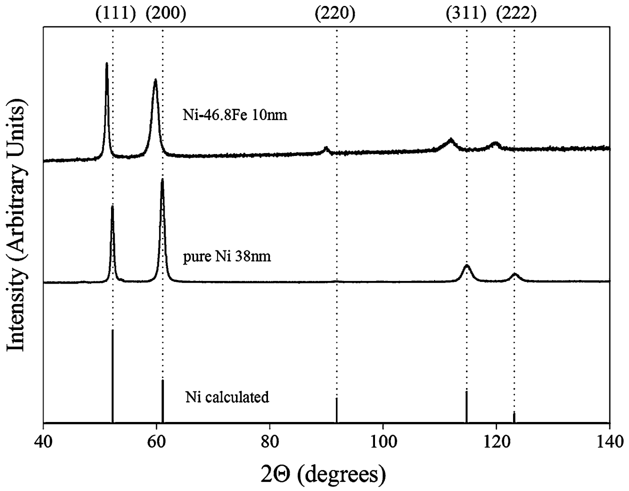

Fig. 2 Typical XRD diffraction profiles (Co Kα radiation) for representative pure Ni (38 nm grain size) and Ni–46.8 wt% Fe (10 nm grain size) nanomaterials

electrodeposition process. A representative nanocrystalline Ni X-ray diffraction pattern is shown in Fig. 2. It may be seen that electrodeposited pure nanocrystalline Ni of 38 nm grain size is face-centered cubic and exhibits a strong (111) (200) fiber texture. In addition, alloying nanocrystalline Ni with Fe is a useful tool to induce grain refinement [16]. To accomplish Ni–Fe alloying, iron chloride and/or iron sulfate was added to the electrolyte along with chelating agents such as sodium citrate to maintain the deposit chemical composition at the desired level. Electrolytic Fe was also added as an anode material so that the solution was continuously replenished with both Ni and Fe cations during the electrodeposition process. In this manner, specimens in the compositional ranges of 0–15 wt% Fe and 47–49 wt% Fe were synthesized. As studied in detail by Cheung et al. [17], Fe alloying of nanocrystalline Ni electrodeposits may induce a transition toward a more random crystallographic texture with increasing iron content/decreasing grain size in the deposits. See Fig. 2 for an XRD pattern taken from a representative Ni–Fe specimen. It can be seen that the Ni–Fe specimen exhibits a (200) texture but is more random than that of the pure Ni deposit. A detailed description of nanocrystalline Ni–Fe electrodeposition is provided by Cheung et al. [13, 16–18].

Unfortunately, most studies that have sought to explore the influence of nanocrystalline grain refinement on mechanical properties have not been able to carry out measurements using standardized tensile tests because the most commonly accepted tensile test protocols call for specimen geometries that exceed the current capabilities of most nanocrystalline material synthesis processes [10]. This has led to (a) the development of non-standard mechanical test methodologies for the evaluation of miniature specimens [e.g., 19], and/or (b) the persistent use of hardness indentation as a proxy for tensile testing [20]. Tensile testing of miniature specimens has inherent limitations that have been addressed in this study, while the relevance of hardness indentation as a tool to assess tensile ductility is questionable because it involves highly localized compressive loading. Therefore, one objective of this study has been the development of a synthesis method to produce specimens large enough for testing in accordance with ASTM E8 [21], arguably the most widely used tensile test in North America. In this manner, the resultant test data might be reliably compared to data from other well-known engineering materials.

In order to extend beyond “thin sheets” and into the geometrical regime of “bulk plate” specimens large enough for testing in conformance with ASTM E8, the target electrodeposit thickness was typically 1 mm, which requires approximately 10–20 h of deposition run time to achieve. From a practical perspective, preventing the formation of processing flaws in the growing electrodeposit for such a lengthy material processing duration was found to be challenging. Hence, one focus of the materials synthesis component of this work was the elimination of electrodeposition processing artifacts. There are a number of key differences between the “early scale-up stage” process originally developed for the production of thin foils and the “later generation” process used to synthesize the bulk samples of the current study. First, steady-state electrolyte surface tension control was implemented as a means to control hydrogen pitting. In aqueous electrodeposition, the preferred cathodic metal reduction reactions are rarely 100% efficient and so some portion of the electric charge is almost always consumed by hydrogen reduction. If the resultant hydrogen outgas fails to detach from the surface of the cathode, then there exists some risk that the bubble will become encapsulated in the growing electrodeposit. This phenomenon is known as “hydrogen pitting” and so best practices in electroplating, and especially electroforming, prescribe the use of wetting agents such as sodium lauryl sulfate to lower the surface tension of the electrolyte so that hydrogen bubbles are encouraged to leave the cathode surface as the deposit grows. Such techniques are typically effective and pit-free plates are readily producible. For the “later generation” process of the present study, the electrolyte surface tension was continuously maintained below 0.03 N/m. Another important difference between the “early scale-up stage” and “later generation” processes is particulate contamination control. Common sources of particulate in the electrolyte include atmospheric dust and feedstock chemical contamination. Because the specimen plate is formed by a deposition process whereby the metal is formed atomic layer upon layer, an initially imperceptibly small geometrical heterogeneity on the electrodeposit surface originating from particulate contamination may gradually grow into a macroscopic protrusion on the plate surface. Such macroscopic defects were less common in electroforming runs of short 1–4 h duration, but commonplace in production runs that exceeded 10 h. Specific strategies to prevent the co-deposition of particulate were therefore implemented including proper enclosure of the electroforming tank, improved feedstock chemical quality, and empirical electrolyte flow pattern optimization combined with fine particulate filtering (1 μm pore size).

All metals were deposited onto Ti cathodes from which they were subsequently stripped to yield free-standing sheets to be cut into specimens for tensile testing. The removal of the nanocrystalline plate was accomplished by mechanically lifting the nanocrystalline plate from the temporary Ti cathode substrate. 152 × 152 mm^2 Ti cathode plates were used as the temporary substrates for the electroformed nanocrystalline materials produced for this study and each electroformed plate was large enough to yield six individual tensile coupons. Figure 3a contains schematic drawings of some of the tensile sample geometries found in the electrodeposited nanomaterials literature [3, 4, 22] alongside the ASTM standard subsize tensile coupon geometry [21] and that used in the current study, while Fig. 3b contains a photograph of a typical electroformed nanocrystalline material plate from the present study from which six individual tensile specimens were cut. All tensile coupons produced for this study were cut using electrical discharge machining with a constant machining template. In other words, the areal shape of all the tensile specimens produced for this study was identical with a 125 mm overall length, 25 mm gauge length, 6 mm gauge width, 35 mm grip section length, and 20 mm grip section width. This geometry was based upon the ASTM standard E8/E8M-09 subsize specimen geometry [21] with the only notable deviation from the standard being the grip section geometry. The grip section width dimension was increased from 10 to 20 mm and the grip length was increased from 30 to 35 mm as a means to prevent slippage in the sample grips; owing to the relatively high hardness and strength of the materials studied, it was found that an increased grip section area was essential for proper specimen clamping. The machined edges of the samples were not polished after cutting, and the free surfaces of all samples were kept in the as-deposited surface condition. 2D surface roughness measurements across an 8 mm scan length on the outer surface of a typical 1-mm thick plate revealed an arithmetic average of the absolute values (R_a) of approximately 1 μm. All tensile tests were carried out at a strain rate of 5 × 10^{-4} s^{-1}. All samples were tested to fracture using a calibrated load cell and the elongation-to-fracture, ε_f, was measured using both a calibrated extensometer and also by measurement of the gauge length before and after testing. Several methods have been used to determine the maximum uniform strain including the graphical method, the Considère criterion, and the point of peak load on the stress–strain curve [23]. In the case of the Considère criterion, different relationships are used depending on whether plastic instability occurs by diffuse necking ($d\sigma/d\varepsilon = \sigma$) such as in the case of round bar, or by localized necking ($d\sigma/d\varepsilon = \sigma/2$) such as in the case of thin flat sheet undergoing plane strain deformation. Many of the samples of the present study exhibited a mixed mode of necking failure. Consequently, the peak load method was used to designate the onset of plastic instability in order to determine the maximum uniform elongation. The elastic component of the maximum uniform strain was assumed to be equivalent to the strain measured from the onset of loading until the 0.2% offset yield point [21] with elastic strain values typically falling within the range of 0.5–1%. The difference between the measured maximum uniform strain (at peak load) and the elastic strain term was then termed the maximum uniform plastic strain.

Results and discussion

Extrinsic effects: processing artifacts and specimen geometry

One key issue stems from our lack of understanding of the effect of processing artifacts on nanostructured material ductility. This is important because the linear extension that may be sustained by a typical mechanical test specimen loaded in tension is not a deterministic material-specific property but instead reflects a distribution (size and orientation) of flaws present in the material in addition to the intrinsic material ductility and specimen size and shape dependencies addressed later in this communication. For instance, Fig. 4a contains tensile engineering stress–strain curves corresponding to six individual tensile bars cut from a single nanocrystalline Ni plate produced using an early scale-up stage electroforming process alongside data gathered from an otherwise identical plate produced using a later generation process with much stricter processing artifact control (Fig. 4b). Both lower absolute values and higher variability in tensile strain-to-fracture measurements are typical of samples cut from plates where defects originating from the process are permitted to form. Fractography revealed that the less ductile specimens (Fig. 4c) often showed signs of brittle fracture (flat region) combined with areas of ductile material flow whereas samples synthesized from a later generation process (Fig. 4d) exhibited few signs of brittle fracture or processing flaws

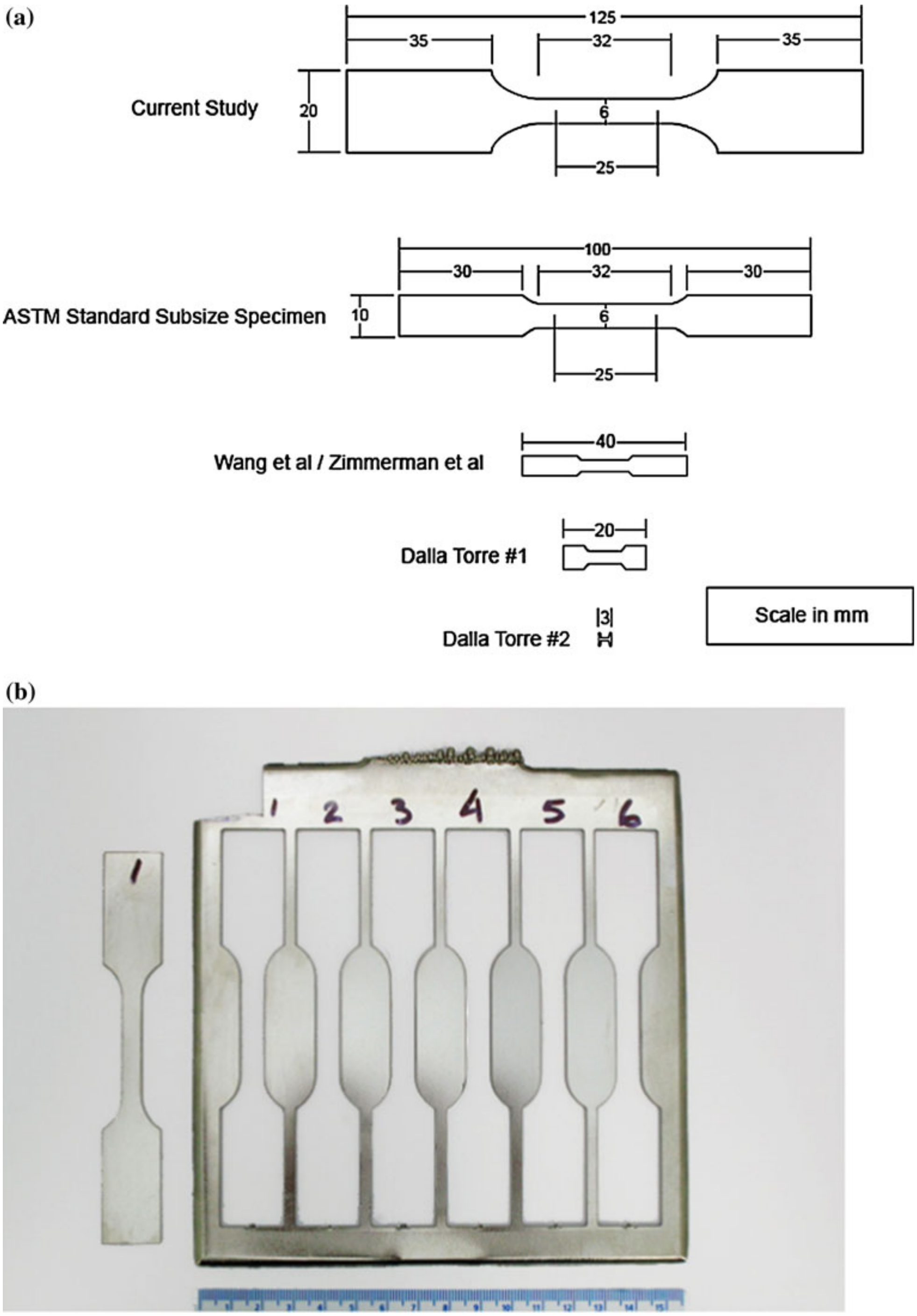

Fig. 3 **a** Schematic diagram of tensile sample geometries used in the current and previous studies (Wang et al. [3], Zimmerman et al. [22], Dalla Torre et al. [4]) on electrodeposited nanocrystalline materials as compared to the ASTM E8 standard subsize tensile test geometry specification [21]. **b** Photograph of a typical electroformed plate from which tensile specimens used in this study were cut alongside a single tensile test specimen (scale in cm)

throughout the volume or along the surfaces. In the face of these process-related challenges, the experimental approach of this study has been to establish a material synthesis technique that is as consistent and artifact-free as possible with the quality control parameter throughout being tensile tests of multiple samples cut from a single plate. Once a consistent sample-to-sample tensile elongation value that exceeded the onset of tensile necking instability was achieved, all relevant process parameters were locked in place and strictly controlled for every

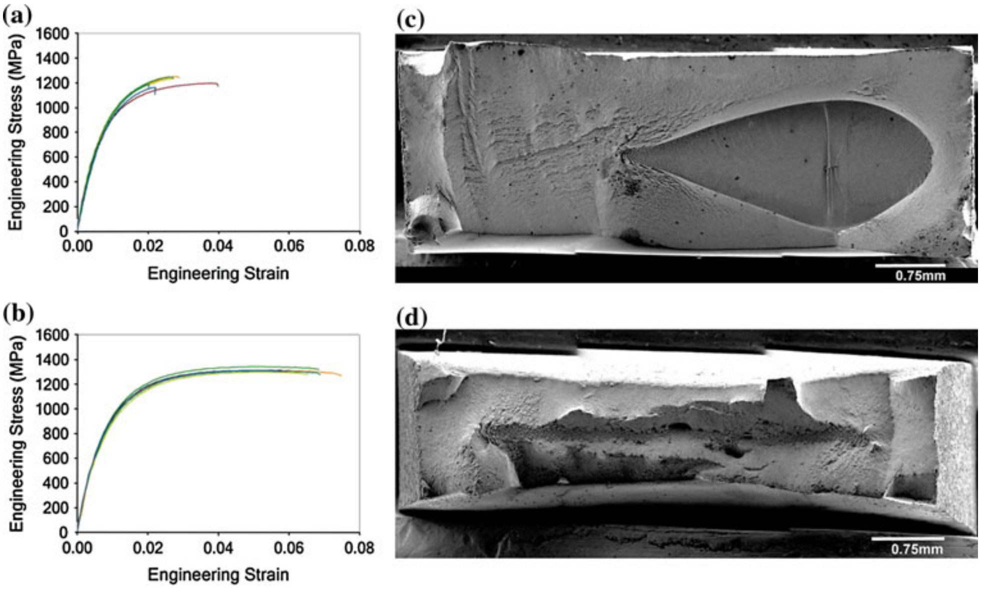

Fig. 4 **a** Tensile engineering stress–strain data from six individual specimens cut from a single plate of material produced using an early scale-up stage electroforming process alongside **b** data from six individual specimens cut from an otherwise identical plate of material produced using a later generation process with much stricter processing artifact control. Scanning electron micrograph images of the fracture surfaces of nanocrystalline Ni tensile samples produced using the corresponding **c** early stage, and **d** later generation processes

subsequent plate produced. Given the probabilistic nature of the fracture event, Weibull distributional analysis was then carried out on statistically significant numbers of samples in order to reveal information on the intrinsic ductility reliability of the materials examined [24].

Another source of confusion in the literature relates to the strong dependency of achievable non-uniform strain (strain past the point of peak load on the stress–strain curve commonly known as the “ultimate tensile stress”) on specimen size and shape. In general, a sample with a larger cross-sectional gauge area will exhibit greater post-uniform elongation in tensile extension than an otherwise identical, geometrically similar sample with a smaller area because of the ability of the larger sample to form a better developed neck, as described by the Unwin equation [25]:

$$\varepsilon_{\mathrm{f}} = \frac{B\sqrt{A}}{L} + \varepsilon_{\mathrm{u}} \tag{2}$$

where ε_{f} is the total elongation-to-fracture, ε_{u} is the uniform elongation, A is the initial gauge cross-sectional area, L is the initial gauge length, and B is a constant. Specimen geometry effects are particularly relevant to the study of nanocrystalline materials because the vast majority of samples studied in the past have been cut from thin sheets or small coupons of feedstock material that prevent the use of standardized mechanical test protocols. For the case of electrodeposited materials, the fracture surfaces typically exhibit dimpling indicative of ductile material flow [4, 26–28] while the macroscopic specimen fracture appearance and measured tensile elongation-to-failure values are oftentimes more in line with those exhibited by intrinsically brittle materials that deform in a glass-like manner [9]. Some have deemed this observation a “paradox” in the study of the mechanical behavior of nanocrystalline materials [29, 30].

Figure 5a shows the relationship between specimen thickness and total achievable strain-to-fracture in tension for 31 nanocrystalline Ni specimens of varying thickness processed in an identical fashion in order to yield similar microstructures and processing defect contents. In the region of lowest thickness between 0.025 and 0.1 mm, the detrimental effect of any minor surface defects (e.g., roughness) or non-uniformity in plate thickness becomes increasingly magnified as the relative size of these defects versus the cross-sectional thickness becomes greater with decreasing thickness. Macroscopically brittle fracture with highly localized necking was observed for specimens in this low thickness regime, as shown in the Fig. 5a inset.

Beginning at approximately 0.1 mm thickness, the tensile elongation-to-fracture of the plates becomes much less sensitive to changes in sample thickness. For these specimens, uniform plastic strain (plastic strain at peak load) values were recorded and are also presented in Fig. 5a. The maximum amount of uniform plastic strain achievable in a tensile test may be considered one measure of a material’s intrinsic ductility and is typically dictated by the microstructure of the material from which it is made. In addition, there is a contribution of loading mode wherein sheet specimens loaded in plane strain may be expected to begin necking later than thicker samples of otherwise identical feedstock material [31, 32]. It may be seen from Fig. 5a that the average uniform plastic strain value exhibited by the ten samples between 0.1 and 0.5-mm thickness was 5.16 ± 0.30% whereas the average uniform plastic strain value exhibited by 13 samples of thickness 0.8 mm and beyond was 4.68 ± 0.35%. The uniform plastic strain

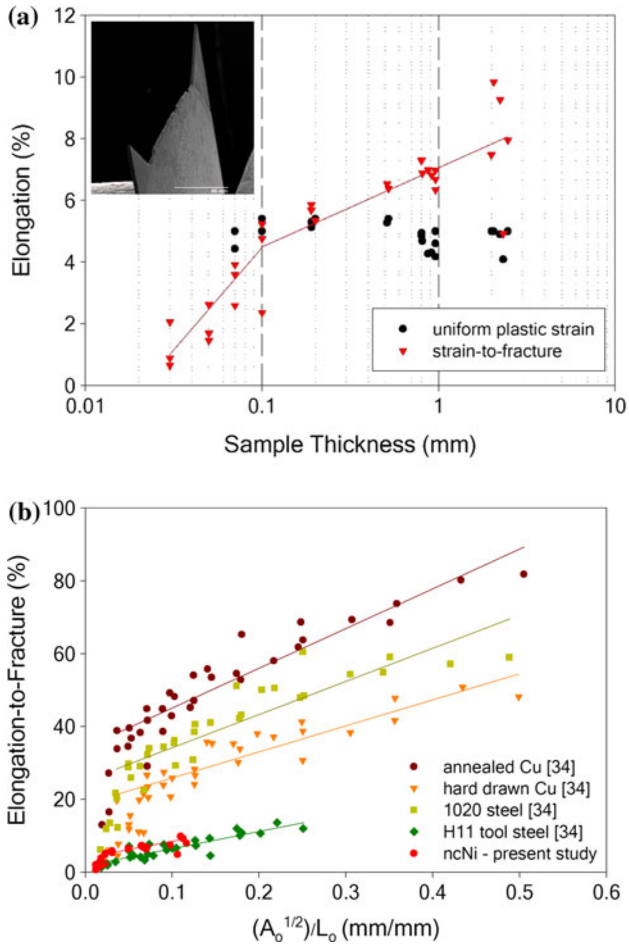

Fig. 5 **a** Quasi-static tensile strain-to-failure and uniform plastic strain as a function of plate thickness for nanocrystalline Ni specimens of similar microstructure, areal shape, and processing method. *Inset* SEM image of a typical thin foil (0.05 mm thickness) sample after tensile testing illustrating the combination of brittle macroscopic fracture morphology and highly localized necking; **b** the geometrical dependency of tensile ductility of nanocrystalline Ni (this study) compared to that exhibited by other standard engineering materials (data from Ref. [34])

values of the thin samples were therefore, on average, approximately 7% higher than the 13 samples of thickness 0.8 mm and beyond. Hence, the thinnest samples appear to exhibit slightly increased uniform plastic strain, likely originating from the fact that these particular samples were loaded in plane strain. Otherwise the uniform plastic strain of the specimens under consideration appears to be relatively invariant across the sample set. This indicates that microstructure does not play a critical role in the observed Fig. 5a geometrical dependence of tensile strain-to-fracture. This observation is consistent with the work of Zhao et al. [33] who carried out similar experiments on ultrafine-grained (100 nm–1 µm grain size) Cu and found that the achievable tensile uniform elongation was independent of specimen thickness. The fact that all samples greater than 0.1 mm thickness in Fig. 5a were intrinsically ductile enough to surpass a point of peak load indicates that the processing artifact content was sufficiently low for final fracture to be initiated by plastic instability.

In Fig. 5b, the nanocrystalline Ni strain-to-fracture data has been re-plotted as a function of $A^{1/2}/L$ as per Eq. 2 alongside the raw data from Kula and Fahey's study on the topic of tensile specimen size and shape effects [34]. Their sample set is useful because the metals examined (copper and steels) are well-known and encompass a broad range of intrinsic tensile properties. Note that the general behavior of nanocrystalline Ni is comparable to that of H-11 tool steel, another high strength material. It can be seen that the samples of large cross-sectional area roughly follow Eq. 2. However, regardless of the material studied, this relationship has a tendency to break down for smaller samples of cross-sectional area below approximately 2 mm^2, or 0.04 mm/mm ($A^{1/2}/L$) on Fig. 5b. The observations of Kula and Fahey are consistent with those of this study and indicate that regardless of the intrinsic ductility of the material under examination, the achievable tensile elongation-to-fracture of thin tensile samples is inherently less predictable as the deformation mode transitions toward distinctly plane strain conditions wherein neck development becomes increasingly geometry/surface-flaw sensitive with decreasing thickness.

The relationship between total elongation-to-fracture and sample geometry of the nanocrystalline Ni samples was also observed to become more unpredictable at the other end of the thickness spectrum (>2 mm), this time in contrast to the behavior of the conventional engineering material benchmarks. Of the five nanocrystalline Ni samples from the highest thickness (>2 mm) regime, four exhibited signs of appreciable ductile material flow, as expected from a relatively defect-free high strength metallic engineering material, while the fifth fractured soon after the onset of post-uniform elongation (indicative of the presence of critical defects). This indicates that, in the case of the thickest nanocrystalline Ni plates, the probability of encountering a critical "ductility controlling" volume defect may become less predictable, and possibly even increase, with increasing plate thickness. On the other hand, it is reasonable to assume that the type, size, orientation and concentration of flaws distributed throughout the volume of the Fig. 5b benchmark engineering material specimens is relatively constant across the entire sample set because all specimens were prepared by slicing samples from starting bar stock material to the desired tensile sample thickness.

These observations invoked the use of Weibull distributional analysis to quantify the variability in ductility data. Weibull analysis is one of the most commonly used tools in reliability analysis, and is based upon a probabilistic “weakest link” depiction of the scatter in the time-to-failure of engineering components. The principles of Weibull distributional analysis [35] are commonly used to interpret fracture stress data from brittle ceramics [36]. However, the method has also been used to characterize the distribution of tensile elongation data taken from aluminum test specimens containing casting defects [37–39] and brittle intermetallic phases [40] from which the ultimate sample fracture is thought to originate. It was assumed throughout that Weibull’s two-parameter mathematical formalism is able to describe the probability distribution of the strain data under examination. The cumulative distribution function of the two-parameter Weibull distribution is given by:

$$F = 1 - \mathrm{e}^{-(\varepsilon_{\mathrm{f}}/\eta)^{\beta}} \tag{3}$$

where F is the failure probability for a given strain-to-fracture ε_{f}, η is the scale parameter, and β is the shape parameter or Weibull modulus. The slope β describes the spread of the data in the probability distribution function and is analogous to the Weibull strength modulus commonly used in the study of brittle ceramics [36]. Figure 6a contains the two-parameter Weibull plot of the tensile strain-to-fracture data from the 31 sample set of nanocrystalline Ni tensile specimens of varying thickness, as indicated by square symbols. Two marked transitions in slope indicate that the geometry-dependent strain-to-fracture data regimes possess unique probability distribution functions. In particular, the probability distribution function shape parameter of the <0.1-mm thick nanocrystalline Ni plate strain-to-fracture values ($\beta = 1.3$) was much smaller than those in the 0.1–1.25 mm thickness regime ($\beta = 5.9$), indicative of a significant drop in ductility reliability for the thinnest specimens. On the other end of the thickness spectrum, data pairs from only five samples from the high thickness (>2 mm) regime were unfortunately not sufficient to calculate a trustworthy Weibull shape parameter, but the drop-off in reliability is nevertheless apparent at the right-hand side of Fig. 6a where this data has been plotted. It is apparent from an examination of Fig. 6a that, as compared to the 0.1–1.25 mm thickness range, one can expect much less predictability in the tensile

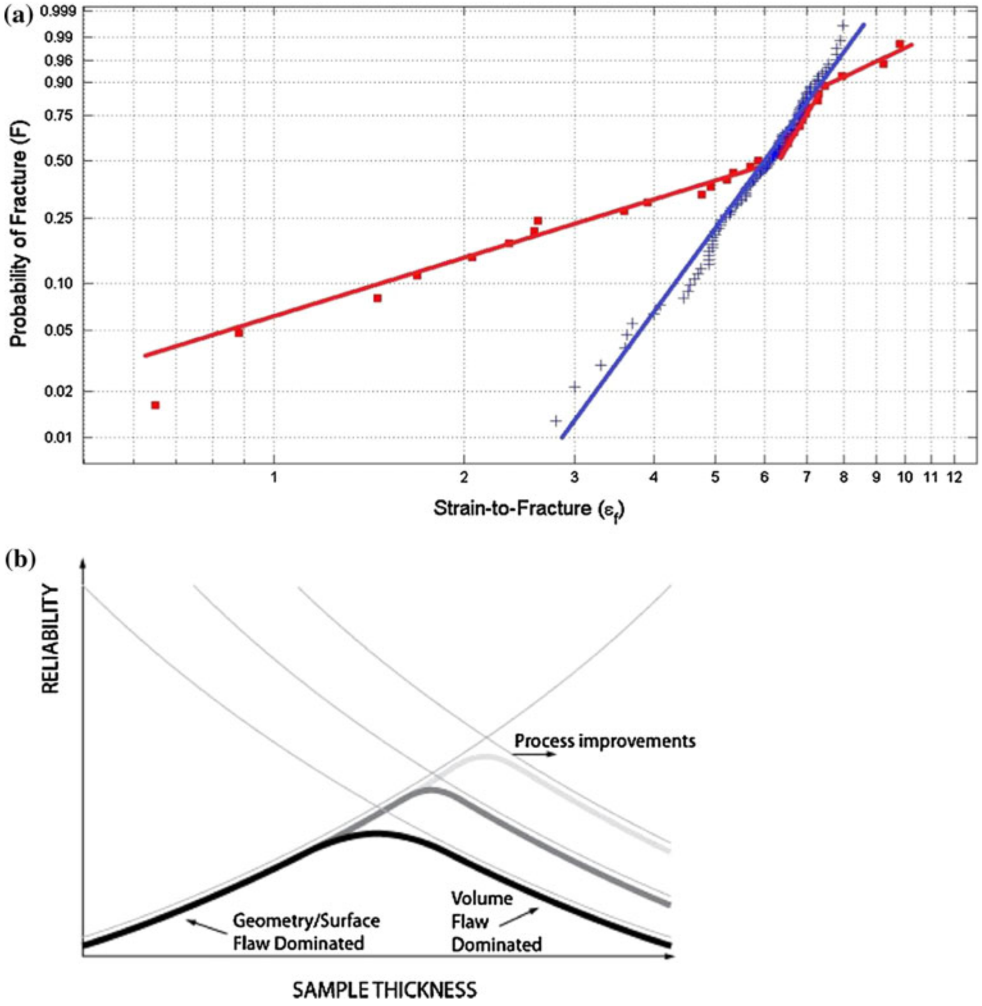

Fig. 6 **a** Two-parameter Weibull fit to strain-to-failure data illustrating the differences in statistical variability between the samples of approximately 1 mm thickness (*crosses*) and the samples of varying thickness from 0.030 to 2.5 mm (*squares*); **b** Schematic diagram depicting the superposition of the geometrical/surface and volume flaw effects that control the tensile ductility variability of electrodeposited nanocrystalline Ni

ductility of either extremely thin monolithic plates of electrodeposited nanocrystalline Ni where the samples are loaded in predominantly plane strain deformation and are highly sensitive to the presence of surface flaws or in extremely thick (greater than approximately 2 mm) samples where the presence of critical ductility controlling volume flaws during lengthy electroforming runs may become significantly more problematic.

This superposition of the geometrical/surface and volume flaw effects that control the achievable tensile elongation of this electrodeposited material system is captured in schematic form in Fig. 6b. Here the reliability of the tensile strain-to-fracture data has been arbitrarily represented on the ordinate axis as a function of sample thickness. Thin samples exhibit plane strain deformation behavior with ultimate fracture being governed by surface flaws and inhomogeneous plate thickness effects. The reliability increases with sample thickness until electroforming process/volume artifacts begin to dominate. Thereafter, the specimen size-dependent material behavior is similar to that observed with engineering ceramics: the larger the specimen, the less ductile it is likely to be. One implication of this behavior is that the region of highest reliability in Fig. 6b can very likely be extended to much higher thickness values (with a commensurate increase in overall achievable tensile elongation as per Eq. 2) via further improvements in electroforming processing flaw elimination. In other words, it would be reasonable to expect that nanocrystalline Ni plates with $A^{1/2}/L$ values that exceed approximately 0.04 mm/mm and produced using a process free of gross volume defects would predictably follow a relationship of the form of Eq. 2. More importantly, as depicted in Fig. 6b, it is anticipated such processing improvements might also increase the overall mechanical reliability in tensile loading, manifested in even higher Weibull shape parameters than those observed in this study.

Optical micrographs of representative nanocrystalline Ni samples spanning the entire range of specimen geometries are shown in Fig. 7, top. The thinnest samples showed fracture along an oblique plane inclined at 55° with respect to the loading axis, gauge width reductions of approximately 2% and gauge thickness reductions of approximately 30–45% (Fig. 7a). This localized necking mode was predominant for the specimens with a width-to-thickness ratio greater than 8 (Fig. 7a, b). On the other hand, the thicker samples showed a transition toward diffuse necking. In particular, the specimens with a width-to-thickness ratio less than 8 exhibited flat fracture after necking down symmetrically around the section normal to the loading direction (Fig. 7c, d), with the thickest samples (Fig. 7d) exhibiting gauge width reductions of approximately 15% and gauge thickness reductions of approximately 30%. The samples of the present study therefore exhibited varying amounts of localized and diffuse necking depending on the sheet thickness. These observations are consistent with the fracture behavior of wide, flat tensile specimens cut from cold worked steel sheet [41] and ultrafine-grained Cu produced by equal-channel angular pressing [33]. As the gauge width-to-thickness ratio increases, there is increased restraint in the width direction such that the contribution of thickness versus width strain to the measured linear extension becomes increasingly asymmetrical and this geometrical constraint plays an important role in the development of the neck [34]. Further commentary on the plastic instability of wide flat tensile specimens under plane strain may be found in [41, 42].

Higher magnification SEM examination of the nanocrystalline Ni fracture surfaces (see Fig. 7, bottom) revealed dimpling indicative of localized ductile plastic

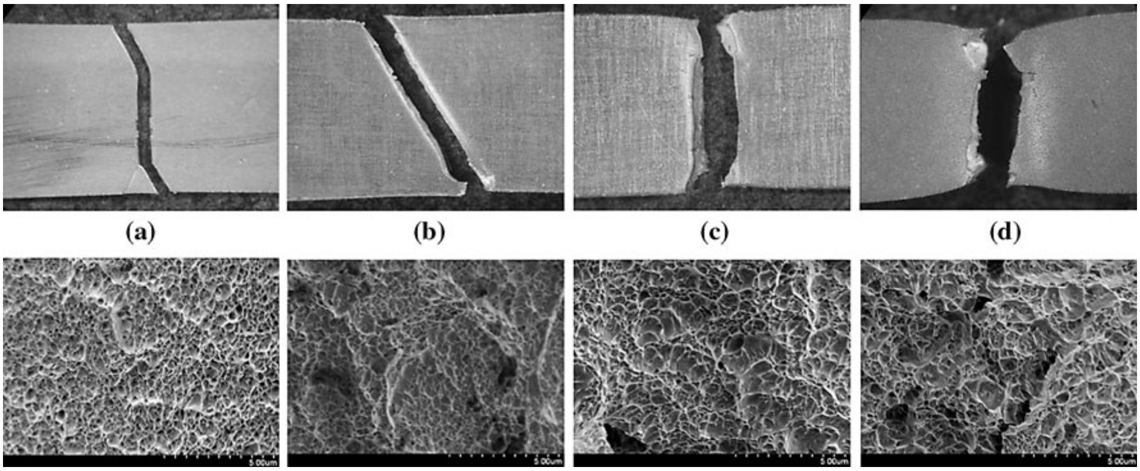

Fig. 7 Optical micrographs of the gauge section of representative specimens illustrating the transition in failure mode with sample thickness paired with SEM images of the corresponding fracture surfaces: **a** <0.1 mm, **b** 0.1–0.5 mm, **c** 0.8–1 mm, **d** 2–2.5 mm. The gauge width of each specimen shown is approximately 6.3 mm. Grain size = 30 nm

flow for all specimens examined, regardless of geometry. The fact that all samples studied exhibited such similar signs of local plasticity, regardless of whether the macroscopic failure mode was brittle or ductile in appearance, supports the view that the observed dependence of ductility on plate thickness is a mechanics effect associated with the size of the deformation zone relative to the plate thickness as the stress state transitions away from plane strain deformation with increasing specimen thickness. Also of interest in Fig. 7 is the observation that the dimples increase in size with plastic strain sustained before fracture. This correlation substantiates the progressive void coalescence aspect of the underlying plastic deformation mechanism(s) [e.g., 28] that ultimately results in dimple formation upon fracture.

Intrinsic ductility

To restrict study to a unimodal failure sample set of high mechanical reliability as per Fig. 6b and minimize the geometry effect in any further considerations, we then tested a statistically significant number of 116 specimens of fixed sample size/shape cut from relatively thick (approximately 1 mm) monolithic nanocrystalline Ni-based electrodeposits produced using a steady-state electroforming process. TEM was performed on selected samples to determine that the tests encompassed an average grain size range of approximately 10–80 nm.

The Weibull plot of the strain-to-fracture data from all 116 tensile specimens is shown as crossed symbols in Fig. 6a alongside the data from the specimens of varying thickness discussed earlier for comparative purposes. Upon examination of the 116 data pair Weibull fit, the first conclusion that can be drawn is that the use of Eq. 3 is sound, with no obvious curvature or marked cusps in the data. Typically, concave curvature in a Weibull plot is a clue to indicate that the three-parameter Weibull should be used instead of the two-parameter [43]. This is not the case for the analysis in question; hence the selection of the two-parameter Weibull distribution to fit the data is considered valid. Second, the Weibull slope of the 116 specimens of constant thickness ($\beta = 6.4$) is similar to that of the 0.1–1.25 mm thickness regime ($\beta = 5.9$) as discussed earlier. This is to be expected since the failure mode and processing method of the 0.1–1.25 mm thick subset of samples is similar to that of the 1-mm thick specimens.

From the perspective of reliability analysis and the design of reliable components, the 116 data pair set in Fig. 6a is of practical interest because it indicates the strain at which a given percentage of samples will fail under quasi-static tensile loading in conformance with ASTM standard E8. Weibull coined these values the “B lives” [35]. For instance, the B1 life for this particular material data set is approximately 2.2%, which implies that 1% of the samples will fail by the time they reach 2.2% elongation in tension. Similarly, the Weibull scale parameter or characteristic strain-to-fracture, η, denotes the strain at which 63.2% of the samples have fractured and is commonly used in Weibull analyses because its value is independent of the slope β [43]. For this particular data set $\eta = 6.38\%$ strain-to-fracture.

Figure 8a contains stress–strain curves from representative nanocrystalline samples from this study alongside coarse-grained pure Ni benchmarks. As seen in Fig. 8b, it was found that the achievable non-uniform strain values recorded from the point of ultimate tensile stress, σ_{UTS}, until final fracture exhibited considerable variability ($\beta = 2.3$) across the 116 sample set, indicating that the processes of damage development during necking are strongly sensitive to the sample-to-sample defect and geometrical variations described earlier. On the other hand, the corresponding maximum uniform plastic strain values were relatively constant at 4.3% ($\beta = 11.3$). Figure 8c contains the same data re-plotted as a function of 0.2% offset yield stress, used as the abscissa because it represents the intrinsic resistance to the onset of plastic deformation of the specimens examined and serves as a proxy for grain size as per Eq. 1. The observation of relatively constant maximum uniform plastic strain holds true for this large set of samples despite a relatively broad dispersion in grain size and associated yield strength. This is somewhat surprising given that microstructural refinement typically results in increasingly limited dislocation storage capacity in the grain interiors of polycrystalline metals, hindering their ability to strain harden. For conventional coarse-grained materials, the manifestation of this progressively inhibited strain hardening capacity with decreasing grain size is that the achievable maximum uniform plastic strain also scales with grain size. Bouaziz [44] and Massart and Pardoen [45] have studied this effect using data recorded on pure Fe, single phase ferritic steels and interstitial free steels with grain sizes in the range of 150 to just below 0.1 μm. Their findings indicated that the maximum achievable uniform plastic strain tends to diminish throughout this microstructural range, and began to plateau with grain refinement below 0.8 μm. Unfortunately, extrapolation into the nanocrystalline regime was not possible with the aforementioned steels. The present study suggests that there is indeed a plateau in the maximum achievable uniform plastic strain for grain sizes in the range of 10–80 nm. To further explore this effect, the strain hardening capacity of the nanocrystalline specimens, $H = \sigma_{\mathrm{UTS}}/\sigma_{\mathrm{Y}}$, has been plotted in Fig. 8d. It can be seen that the strain hardening capacity was found to decrease with decreasing grain size, as might be expected from the behavior of conventional coarse-grained polycrystalline

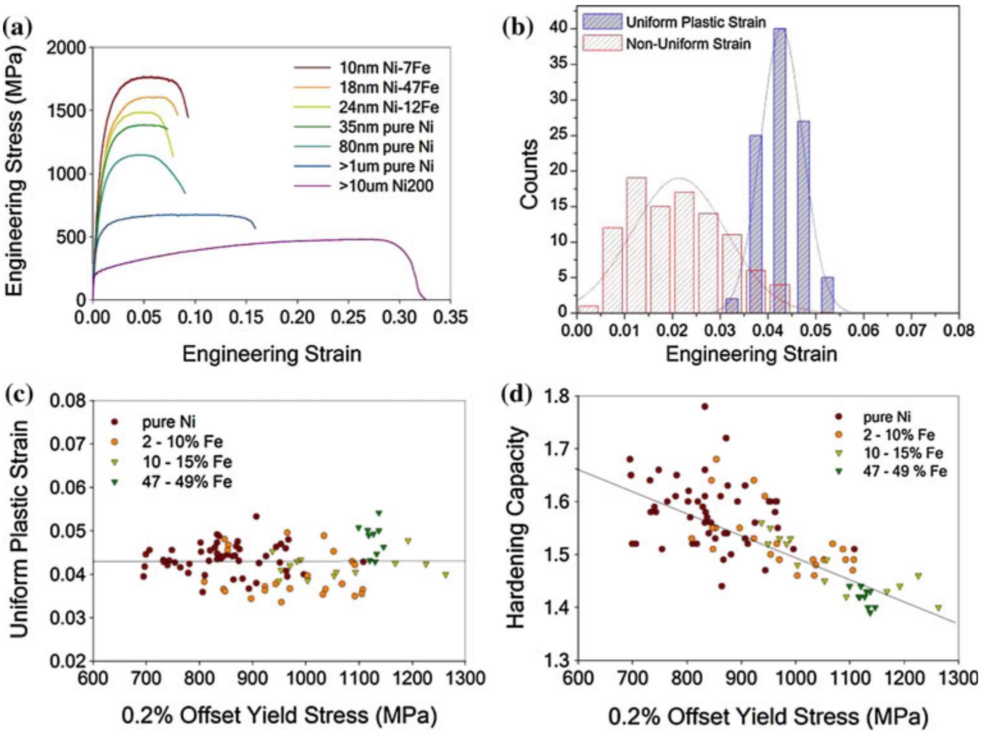

Fig. 8 **a** Representative tensile engineering stress–strain curves with average grain sizes and compositions provided in the legend. All samples electrodeposited except for the Ni-200 standard; **b** Maximum uniform plastic and non-uniform strain distributions for 116 nanocrystalline Ni-based specimens of equivalent geometry and spanning average grain size values from 10 to 80 nm; maximum uniform plastic strain (**c**) and hardening capacity (**d**) plotted as a function of yield strength which serves as a proxy for grain size as per Eq. 1

materials. Yet despite this correlation, the hardening capacity has no apparent impact on the intrinsic ductility as measured by uniform plastic strain. Such differences in strength parameters among the tested samples have made the observation of constant maximum uniform plastic strain for this large sample set even more significant.

In ductile polycrystalline metals, the onset of plastic instability may be considered a signpost for the beginning of micro-damage formation followed by pronounced strain localization as the sample is deformed beyond the point of peak tensile loading. In coarse-grained materials, such damage usually takes the form of voids that typically develop at the interfaces between second phase particles and the matrix material, or at the grain boundaries. For this case, the synthesis conditions are such that damage formation originating primarily from second phase particles is unlikely. On the other hand, the underlying physical processes that govern the plastic flow, damage development, and subsequent fracture of nanocrystalline materials are primarily grain boundary- and/or triple junction-mediated [46]. In the case of macroscopically "brittle" fracture, for instance, small-scale damage takes the form of nanovoids that nucleate and converge at the crystal interfaces, ultimately resulting in brittle, intergranular fracture. On the other hand, if plastic flow and diffusion are intense in the proximity of the interfaces, the as-formed flat interfacial nanovoids gradually transform into pores, and with continued external loading, these pores progressively coalesce to form the dimples that we ultimately observe on the fracture surfaces of macroscopically "ductile" specimens, e.g., Figure 7. In other words, regardless of whether the macroscopic failure mode is "ductile" or "brittle", the first stage of nanocrystalline material damage formation remains the same: localized interfacial decohesion leading to the formation of nanovoids situated at the grain boundaries and/or triple junctions [46]. While the specific physical mechanisms that contribute to deformation-induced damage nucleation and growth in ductile nanocrystalline materials are currently a matter of intense debate [30, 47, 48], these results indicate that, within the grain size range of 10–80 nm, this interfacial damage formation seemingly does not depend on grain size nor bulk material strength (as governed by grain size) but is instead a strain-controlled phenomenon that can and would be better defined by a critical plastic strain, namely the maximum uniform plastic strain level.

Conclusions

This study on the ductility of electrodeposited nanocrystalline metals has shown the following:

(1) The impact of electroforming process control on both the absolute value and variability of achievable tensile elongation is strong. High variability in tensile strain-to-fracture is seen in samples cut from plates where defects originating from the process were

permitted to form in the electrodeposit. On the other hand, samples originating from a strictly controlled electroforming process were not only more ductile overall, but were more consistent from a sample-to-sample tensile strain-to-fracture perspective.

(2) The “paradox” between macroscopic glass-like fracture and microscopic ductile fracture surfaces is mainly a mechanics (geometry) effect.

(3) Necking elongation obeys similar processing quality and geometrical dependencies as in conventional engineering metals.

(4) Unlike conventional engineering metals, intrinsic ductility (as measured by maximum uniform plastic strain) is unexpectedly independent of microstructure over the grain size range 10–80 nm. This indicates that the underlying physical processes of grain boundary-mediated damage development are strain-oriented phenomena that can be best defined by a critical plastic strain regardless of the strength of the material as a whole.

Acknowledgement The authors gratefully acknowledge the generous support of the Natural Sciences and Engineering Research Council of Canada, Industry Canada (Technology Partnerships Canada program), National Research Council (Industrial Research Assistance Program), Ontario Research Fund, and the U.S. Department of Defense Strategic Environmental Research and Development Program project PP-1152.

References

1. Hall EO (1951) Proc Phys Soc Lond B64:747
2. Petch NJ (1953) J Iron Steel Inst 173:25
3. Wang N, Wang Z, Aust KT, Erb U (1995) Acta Metall Mater 43(2):519
4. Dalla Torre F, Van Swygenhoven H, Victoria M (2002) Acta Mater 50:3957
5. Hansen N (2005) Adv Eng Mater 7(9):815
6. Weertman JR (2007) In: Koch CC (ed) Nanostructured materials, 2nd edn. William Andrew, Norwich, p 397
7. El-Sherik AM, Erb U, Palumbo G, Aust KT (1992) Scr Metall Mater 27:1185
8. Erb U, Palumbo G, Zugic R, Aust KT (1996) In: Suryanarayana C et al (eds) Processing and properties of nanocrystalline materials. TMS, Warrendale, p 93
9. Koch CC (2003) J Metastab Nano Mater 18:9
10. Koch CC (2007) In: Koch CC et al (eds) Structural nanocrystalline materials. Cambridge University Press, Cambridge, p 134
11. Zhao Y, Zhu Y, Lavernia EJ (2010) Adv Eng Mater 12(8):769
12. Erb U, El-Sherik AM (1994) US Patent #5,352,266
13. Erb U, El-Sherik AM, Cheung CKS, Aus MJ (1995) US Patent #5,433,797
14. El-Sherik AM, Erb U (1995) J Mater Sci 30:5743. doi:10.1007/BF00356715
15. McMahon G, Erb U (1989) Microstr Sci 17:447
16. Cheung C, Palumbo G, Erb U (1994) Scr Metall Mater 31(6):735
17. Cheung C, Djuanda F, Erb U, Palumbo G (1995) Nanostr Mater 5(5):513
18. Cheung C, Nolan P, Erb U (1994) Mater Lett 20:135
19. Legros M, Elliott BR, Rittner MN, Weertman JR, Hemker KJ (2000) Phil Mag A 80(4):1017
20. Brooks I, Lin P, Palumbo G, Hibbard GD, Erb U (2008) Mater Sci Eng A 491:412
21. ASTM Standard E8/E8M-09 (2009) ASTM International, West Conshohocken
22. Zimmerman AF, Palumbo G, Aust KT, Erb U (2002) Mater Sci Eng A 328:137
23. Dieter GE (1988) Mechanical metallurgy, SI metric edn. McGraw-Hill, London, p 290
24. Weibull W (1939) Ingen Vetenskaps Acad Proc 151:153
25. Dieter GE (1985) In: Metals handbook, vol 34, ASM International, Metals Park, p 12
26. Erb U, Aust KT, Palumbo G (2007) In: Koch CC (ed) Nanostructured materials, 2nd edn. William Andrew, Norwich, p 235
27. Li H, Ebrahimi F (2006) Acta Mater 54:2877
28. Hasnaoui A, Van Swygenhoven H, Derlet PM (2003) Science 300:1550
29. Shan Z, Knapp JA, Follstaedt DM, Stach EA, Wiezorek JMK, Mao SX (2008) Phys Rev Lett 100:105502
30. Ovid’ko IA, Sheinerman AG, Skiba NV (2011) Acta Mater 59:678
31. Koch CC, Youssef KM, Scattergood RO, Murty KL (2005) Adv Eng Mater 7(9):797
32. Misra A, Zhang X, Hammon D, Hoagland RG (2005) Acta Mater 53:221
33. Zhao YH, Guo YZ, Wei Q, Dangelewicz AM, Xu C, Zhu YT, Langdon TG, Zhou YZ, Lavernia EJ (2008) Scr Mater 59:627
34. Kula EB, Fahey NH (1961) Mat Res Stand 1:631
35. Weibull W (1951) Appl Mech 18:293
36. ASTM Standard C1239-07 (2007) ASTM International, West Conshohocken
37. Teng X, Mae H, Bai Y, Wierzbicki T (2008) Eng Fract Mech 75:4610
38. Teng X, Mae H, Bai Y, Wierzbicki T (2009) Eng Fract Mech 76:983
39. Hashemi H, Raiszadeh R (2009) J Appl Sci 9(11):2115
40. Zahedi H, Emamy M, Razaghian A, Mahta M, Campbell J, Tiryakioglu M (2007) Metall Mater Trans A 38:659
41. Nadai A (1950) Theory of flow and fracture of solids, vol 1. McGraw-Hill, New York, p 319
42. Ragab AR, Bayoumi SE (1999) Engineering solid mechanics. CRC Press, Boca Raton, p 738
43. Abernathy RB (1996) The new Weibull handbook, 4th edn. Gulf Pub. Co, North Palm Beach
44. Bouaziz O (2009) Adv Eng Mater 11(10):767
45. Massart TJ, Pardoen T (2010) Acta Mater 58:5768
46. Ovid’ko IA (2007) In: Koch CC et al (eds) Structural nanocrystalline materials. Cambridge University Press, Cambridge, p 280
47. Bringa EM, Traiviratana S, Meyers MA (2010) Acta Mater 58:4458
48. Bulatov VV, Wolfer WG, Kumar M (2010) Scr Mater 63:144